A hybrid deep learning approach for gland segmentation in prostate histopathological images

A hybrid deep learning approach for gland segmentation in prostate histopathological images

Massimo Salvi,[a,*] Martino Bosco,[b] Luca Molinaro,[c] Alessandro Gambella,[c] Mauro Papotti,[d] U Rajendra Acharya,[e,f,g] and Filippo Molinari,[a]

[a] Politecnico di Torino, PoliTo[BIO]Med Lab, Biolab, Department of Electronics and Telecommunications, Corso Duca degli Abruzzi 24, Turin, Italy, 10129

[b] San Lazzaro Hospital, Department of Pathology, Via Petrino Belli 26, Alba, Italy, 12051

[c] A.O.U. Città della Salute e della Scienza Hospital, Division of Pathology, Corso Bramante 88, Turin, Italy, 10126

[d] University of Turin, Division of Pathology, Department of Oncology, Via Santena 5, Turin, Italy, 10126

[e] Department of Electronics and Computer Engineering, Ngee Ann Polytechnic, Singapore

[f] Department of Biomedical Engineering, School of Science and Technology, SUSS University, Clementi, 599491, Singapore

[g] Department of Bioinformatics and Medical Engineering, Asia University, Taiwan

CORRESPONDENCE TO:

Ing. Massimo Salvi, PhD

Biolab, Department of Electronics and Telecommunications, Politecnico di Torino, Torino, Italy

Corso Duca degli Abruzzi, 24 - 10129 Torino, ITALY

Phone: +39 011 090 4207

Fax: +39 011 090 4217

E-mail: massimo.salvi@polito.it

Abstract

Background: In digital pathology, the morphology and architecture of prostate glands have been routinely adopted by pathologists to evaluate the presence of cancer tissue. The manual annotations are operator-dependent, error-prone and time-consuming. The automated segmentation of prostate glands can be very challenging too due to large appearance variation and serious degeneration of these histological structures.

Method: A new image segmentation method, called RINGS (Rapid IdentificatioN of Glandural Structures), is presented to segment prostate glands in histopathological images. We designed a novel glands segmentation strategy using a multi-channel algorithm that exploits and fuses both traditional and deep learning techniques. Specifically, the proposed approach employs a hybrid segmentation strategy based on stroma detection to accurately detect and delineate the prostate glands contours.

Results: Automated results are compared with manual annotations and seven state-of-the-art techniques designed for glands segmentation. Being based on stroma segmentation, no performance degradation is observed when segmenting healthy or pathological structures. Our method is able to delineate the prostate gland of the unknown histopathological image with a dice score of 90.16% and outperforms all the compared state-of-the-art methods.

Conclusions: To the best of our knowledge, the RINGS algorithm is the first fully automated method capable of maintaining a high sensitivity even in the presence of severe glandular degeneration. The proposed method will help to detect the prostate glands accurately and assist the pathologists to make accurate diagnosis and treatment. The developed model can be used to support prostate cancer diagnosis in polyclinics and community care centres.

Keywords: glands segmentation, digital pathology, computer-aided image analysis, prostate cancer, deep learning.

1. Introduction

Prostate cancer is the most common cancer in men and the fifth cause of cancer-related deaths globally [1], [2]. Deeper understanding of the type and stage of prostate cancer is necessary to provide accurate treatment. More than 70% of men above 70 years develop prostate cancer, but only 10% of them are fatal [3], [4], [5]. Therefore, there is an urgent need for an accurate prognostic factor stratification of this cancer. Nowadays, the Gleason score assessment performed on prostate biopsies is considered as the gold-standard technique.

The Gleason score is a five-grade based score that evaluates the architecture of neoplastic glands. It is a relatively easy method of prostate cancer prognostic assessment, and it is routinely performed by almost every pathology units worldwide. The primary issue about Gleason score is the reproducibility of its outcomes. Several reports in the literature have highlighted the subjectivity in the manual Gleason score assessment and hence causes the variance in the assessment [6], [7], [8]. In recent years, follow-up emerged as an alternative to prostatectomy in patients with low Gleason Score; consequently, reproducibility of this parameter is now relevant not only for the prognosis but also for establishing the correct therapeutic approach. As stated before, the only parameter considered by Gleason score assessment is the architectural pattern of neoplastic glands (Figure S1). However, several patterns present overlapping features and can be wrongly graded, causing wrong outcomes [9], [10], [11]. Gleason score is also a time-consuming reporting activity for the pathology units. Pathologists need to go through *twelve* biopsies for one patient and need to present a report with details of cancer features (e.g., including at least Gleason score, Gleason grade, length of the biopsy, length of the tumor, percentage of the tumor-affected tissue, continuity/discontinuity of the lesion, ratio of affected biopsy cores with the number of the total cores) [12], [13].

In this challenging panorama, digital prostate gland segmentation may offer crucial support to the Gleason score assessment. The application of digital analysis and image segmentation to the field of pathology may help to accurately identify specific structures, such as prostatic glands, and can help to improve pattern recognition [14], [15]. The support of an automated image analyzer would increase the identification of prostatic glands - both physiological and neoplastic – and the interpretation of their arrangement. The application and implementation of automated segmentation of glands in prostate cancer cells will overcome the subjectivity issue and help to boost the accuracy of detection. Recently, many methods have been proposed to the development

of automatic glands segmentation techniques with the aim to improve both the accuracy and the efficiency in histopathological image analysis [16], [17]. The prostate glands segmentation is a challenging task because of variability in shape, dimension and internal architecture of glands especially in pathological conditions (see Supplementary Material). All current deep learning-based approaches formulate this detection problem as a direct segmentation task. The operator manually annotates the glands contours, and the convolutional neural network (CNN) is then trained to recognize the glandular areas. However, training a deep network to detect cancerous patterns is not a trivial task as it is not easy to obtain accurate manual annotations due to the presence of severe glandular degeneration.

In this paper, a novel glands segmentation strategy for histological images is presented. The main contribution of this paper can be summarized as follows:

- We propose a hybrid deep learning framework that combines the accuracy of an active contour model with the semantic segmentation performed by a CNN. In particular, traditional and deep learning techniques are employed to create a hybrid image in which the contrast between glands and stroma is greater than the original image. Then, a softmax-driven active contour model is applied to detect all the prostate glands.
- We develop an effective approach based on stroma segmentation to accurately detect the contours of prostate glands even in the presence of severe glandular degeneration. By complementing the stroma mask, we are able to bypass the limitations of the current methods.
- We publicly release a dataset of 1500 H&E (hematoxylin & eosin) stained images of prostate tissue along with 18851 annotated glands. For each image of the dataset, we also provide the manual annotation of cancer tissue.
- An extended validation is performed by comparing the proposed approach with the most recent state-of-the-art techniques. Our algorithm obtains highly satisfactory results and outperforms all the compared methods [18], [19], [20], [21], [22], [23], [24].

The rest of this paper is organized as follows: Section 2 presents an overview of the current approach for prostate glands segmentation; Section 3 provides an exhaustive description of the proposed approach; Section 4 and 5 report and discuss the experimental results.

2. Related Works

Recently, many methods have been proposed for glandular structures segmentation. Farjam et al. [18] used a combination of Gaussian filters to extract the texture features of the prostate tissue. Then, a k-means clustering is used to extract the glands boundaries. Texture-based approaches generally perform badly in the case of high stain intensity variability images and do not take into account the spatial information between epithelial nuclei and lumen. To overcome this problem, different algorithms have been developed to exploit the relationship between nuclei/stroma combined with the gland morphology. Naik et al. [19] implemented a level-set for prostate gland segmentation. The initial contour of the curve is detected by a Bayesian classifier that identified all the lumen regions. Then, an energy functional is defined to obtain the minimum energy when the level set is near the epithelial nuclei. If properly initialized, the level-set is used to obtain the satisfactory segmentation. This property also defined its main limitation, which is the level-set initialization. This class of algorithms may generate an inaccurate segmentation due to incorrect or missing initial level-sets (e.g., in the case of glands with no visible lumen). Peng et al. [20] employed a color decomposition and a principal component analysis to detect the four main components of the histological tissue (lumen, nuclei, stroma and cytoplasm). Then, a post-processing strategy is applied to identify the gland boundaries. This method achieved a reasonable gland detection on healthy tissues but, in the presence of tumoral patterns, a significant drop in the segmentation accuracy is observed. Nguyen et al. [21] used k-means classification based on LAB color space information to classify pixels as nuclei, cytoplasm, lumen and stroma. The method then merged the lumen, cytoplasm and nuclei pixels to extract the glandular regions. Singh et al. [22] trained a logistic regression classifier to detect stoma, gland and lumen pixels. Then, a heuristic process is applied to obtain the final gland segmentation. These last two methods performed well on structures containing lumen, but they failed to segment the glands with discontinuous/absent lumina (as in the case of pathological conditions).

Recently, deep learning methods achieved state-of-the-art performance in many fields of medical imaging [25], [26], [27], including digital pathology image analysis [28], [29], [30]. Ren et al. [23] proposed a convolutional neural network (CNN) for binary prostate gland segmentation in histopathological images. The semantic segmentation is performed using an encoder network followed by a decoder network. Both the encoding and decoding network contained 10 convolutional layers. The input layer of the CNN had a dimension of 480x360x3. Bigger images

are segmented using a sliding window approach. Using this strategy, the authors obtained higher performance compared to the previously published works. Xu et al. [24] focused on the gland segmentation task using three-channels of CNN. One channel is designed for segmenting background from foreground pixels. The second channel detects gland boundaries while the third channel is employed for the detection of individual glands. The outputs of these three channels are fused by a CNN to obtain the final segmentation result. All the CNNs are based on the VGG16 model. In particular, the architecture consists of five pooling structure with an image input size of 400x400x3. These deep learning methods, however, did not address the issues of segmenting glands with no visible lumen explicitly. Gland detection may perform well for benign and well-shaped glands, but the deep network hardly detects glands accurately in malignant cases.

3. Materials and Methods

In this paper, an automated method called RINGS (Rapid IdentificatioN of Glandural Structures) is presented. The RINGS algorithm is a fully automated method developed for prostate glands segmentation in H&E stained images. The flowchart of our approach is illustrated in Figure 1. Our method consists of *three* steps: image normalization, object detection (based on deep networks and traditional techniques) and hybrid segmentation. A detailed description of the RINGS algorithm is provided in the next section.

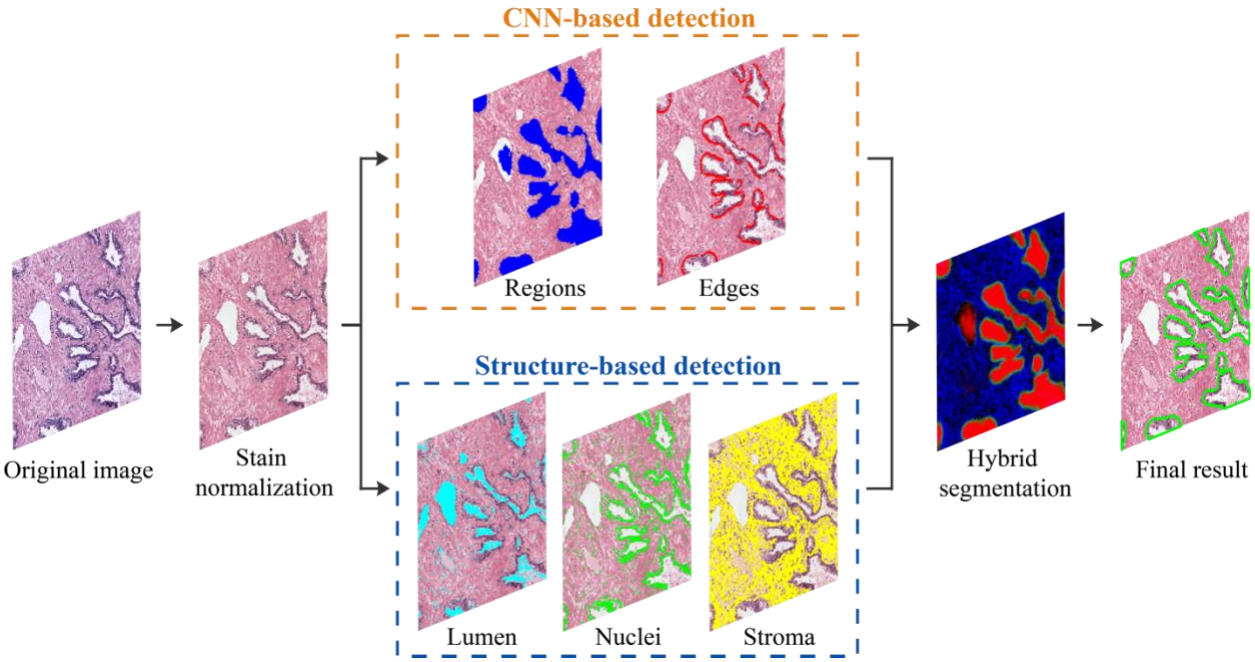

Figure 1. Schematic representation of RINGS algorithm. Starting from the RGB image, a stain normalization method is applied. A deep neural network is employed to detect both regions and contours of glands while cellular structures (lumen, nuclei, and stroma) are found using traditional methods. Then, the hybrid segmentation combines all these information to obtain the final contours of glands.

3.1 Human prostate histology

The whole-slide images of prostate biopsy specimens of 150 male patients (median age 63.2 years, range 41-86 years) were collected at the Division of Pathology, Department of Oncology, Turin, Italy. The histological tissues were collected by biopsy, formalin-fixed and paraffin-embedded, serially sectioned to 5 μm, and stained with H&E. Digital images were scanned with a magnification of x100 (conversion factor: 0.934 μm/pixel) using a Hamamatsu NanoZoomer S210 Digital slide scanner. Ten images of 1500x1500 pixels were extracted from each patient (n=150), for a total of 1500 images. Our database was then divided into two subsets: TRAIN (1000 images) and TEST (500 images). Manual annotations of the contours of the glands (n=18851) were generated after consent by two of us (MB and LM). Table 1 shows the details of the dataset composition. The image dataset, along with the annotations are available at https://data.mendeley.com/datasets/h8bdwrtnr5/draft?a=d40d333e-1a25-4a30-a446-20299d773c3a

Table 1 Dataset composition.

Dataset	#Patients	#Images	#Annotations
TRAIN	100	1000	12924
TEST	50	500	5927

3.2 Image normalization

The first preprocessing step of the proposed pipeline is image normalization. Starting from the original RGB image, the RINGS algorithm performs the stain normalization method which we developed in our previous work [31]. The procedure of stain normalization involves transforming a source image I into another image I_{NORM}, through the operation $I_{NORM} = f(I, I_{REF})$, where I_{REF} is a reference image and $f(\cdot)$ is the function that applies the color intensities of I_{REF} to the source image. This is a crucial step as the appearance of the histological specimen often suffers from large variability due to the chemical reaction of dye used during staining and operator's ability. In this

context, the normalization of color appearance is fundamental in the development of automated solutions for quantitative analysis of histological images [32], [33]. Color normalization helps to standardize the stain appearance of a source image respect to a reference image. Figure 2 shows the color normalization process of a sample image.

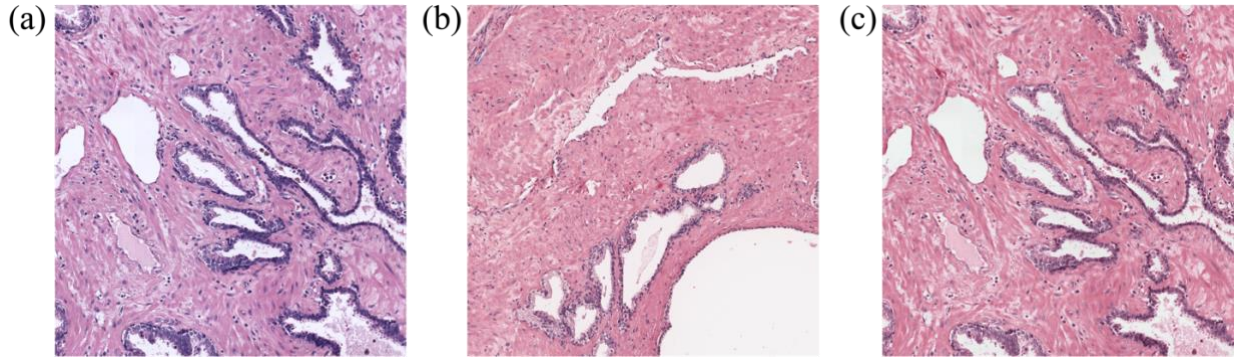

Figure 2. Stain normalization performed by the RINGS algorithm. The normalized image is obtained by applying the color intensities of the reference image to the source one. (a) original source image, (b) reference H&E-stained image, (c) normalized source image.

3.3 Objects detection

This section describes the object detection strategies used to segment the prostate glands contours. The RINGS algorithm applies *two* different processing steps to identify the glandular regions: i) CNN-based detection, ii) structures-based detection.

3.3.1 CNN-based detection

The proposed pipeline implements a convolutional neural network (CNN) to segment the prostate glands. In particular, a UNET architecture with ResNet34 backbone [34] is employed to perform semantic segmentation. The overall network architecture is shown in Figure 3. This deep network is composed of an encoder and a decoder structure. The encoder network, based on the ResNet34 architecture, downsamples the spatial resolution of the input image to obtain a low-resolution feature mapping. The decoder network is then obtained by mirroring the encoding part using transposed convolutions. The aim is to project all the discriminating characteristics (lower resolution) learned from the encoder onto the pixel space (higher resolution) to obtain a dense classification. The output of the network is a probability map that assigns to each pixel a probability of belonging to a specific class. The entire network is trained on a three-class problem,

giving the 480x480 RGB images as input and the corresponding labeled masks as the target. In order to train the network, the outline of each prostate gland is extracted from the manual mask. Then, a dilation is performed with a disk of 2-pixel radius to obtain a binary mask of glands contours. Finally, pixels are labeled in three classes: (i) glands, (ii) glands boundaries, and (iii) background. The reason for choosing both object and edge detection is to define the spatial limit of each gland based on the information on the location and contour of each object. Previous studies have shown that this joint effort performs better than the single approach [17], [24].

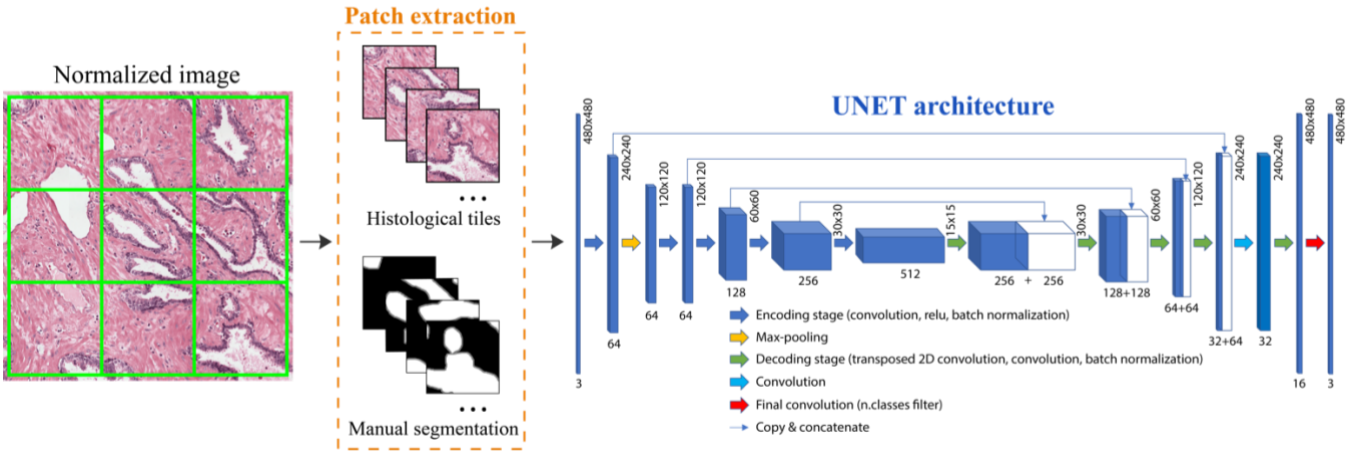

Figure 3. Patch extraction and architecture of the deep network employed in this work. The normalized image is divided into non-overlapping patches of 480x480x3. Then, a three-class UNET is adopted to perform prostate glands segmentation using Keras framework.

To solve the problem of class imbalance, our network's loss function is class-weighted by taking into account how frequently a class occurs in the training set. This means that the least represented class (glands boundaries) will have a greater contribution than the more represented one (glands and background) during the weight update. The class weight is calculated as follows:

$$f_{classX} = \frac{1}{N}\sum_{i=1}^{N}\frac{pixel_{classX}}{area(I)} \qquad X = 1,2,3 \tag{1}$$

$$class_{weightX} = \frac{median(f_{class1}, f_{class2}, f_{class3})}{f_{classX}} \tag{2}$$

where I represents the current image, N is the total number of images, and f_{classX} is the class frequency of the generic class X.

The encoding network is pre-trained on ILSVRC 2012 ImageNet [35]. During the training process, only the decoder weights are updated, while the encoder weights are set to non-trainable. This strategy allows transferring the knowledge acquired from a previous task (ImageNet) to solve a new problem (glands segmentation). This approach is useful both to overcome the problem of small datasets and to reduce the training time [36]. Moreover, on-the-fly data augmentation is implemented by applying random transformations (i.e., flipping, shifting, rotation) both to the input image and to the corresponding encoded mask. Real-time data augmentation prevents network overfitting and makes the model more robust by increasing the amount of data available during training. The deep network was trained on 9000 patches (9 patches for each training image) with a mini-batch size of 128 and an initial learning rate of 10^{-3}. Categorical cross-entropy and the Adam optimizer are employed as a loss and optimization function, respectively. Finally, the maximum number of epochs was set to 30, with a validation patience of 10 epochs for early stopping of the training process. The total training time was 17 hours on a dedicated workstation equipped with a GeForce 1080Ti, 128 GB of RAM, and a 4.1 GHz ten-core CPU.

To preserve the information near the boundaries of the image, the RINGS algorithm applies a specific procedure to build the CNN softmax. Briefly, a mirror border is synthesized in each direction and a sliding window approach is employed to build the probability map. To give the reader the opportunity to observe the entire procedure, we added a detailed description along with a summary figure in the Supplementary Material.

3.3.2 Structure-based detection

The structure-based detection helps to identify *three* basic cellular components within the image: lumen, nuclei and stroma. In order to detect the lumen area (i.e., uncolored regions), the normalized image is converted to grayscale and Wiener filtered and finally, a fixed threshold of 240/255 (equal to 94% of the image maximum) is applied to segment all the white regions.

All detected white regions are erased to process only H&E stained structures (nuclei and stroma). The next step of the RINGS algorithm is the detection of the cellular regions of interest: nuclei and stroma. In order to perform this task, the stain separation proposed in our previous work [31] is employed to isolate the hematoxylin (nuclei) and eosin (stroma).

Cellular nuclei are identified using an improved version of MANA (Multiscale Adaptive Nuclei Analysis) algorithm [37]. In particular, a custom object-based thresholding is applied to the

hematoxylin channel (nuclei) obtained in the previous step. Let's consider a grayscale image with pixel intensities expressed by integer numbers between 0 and 255. For each possible threshold point $T \in [0, 255]$, we calculated the probability of having gray values equal to or lower than T (p_0) and higher than T (p_1). Hence, p_0 and p_1 are related to the background and nuclei distribution, respectively. Then, the following energy function is computed:

$$E(T) = p_0^2 * var_0 * log(var_0) + p_1^2 * var_1 * log(var_1) \quad (3)$$

where var_0 and var_1 are the variances of the probability functions of the two classes p_0 and p_1. The optimal thresholding point is then found by minimizing the energy function E in Eq. (3). The result of nuclei segmentation is illustrated in Figure 4.

In order to identify stroma regions, k-means clustering is applied to the eosin channel. After min-max scaling, a fast k-means algorithm [38] is employed with a number of clusters equal to 2: stroma and background. The initial centroids for clustering are respectively the pixel with the highest and lowest intensity within the image. After k-means, stroma pixels correspond to the cluster with the highest mean intensity (Figure 4).

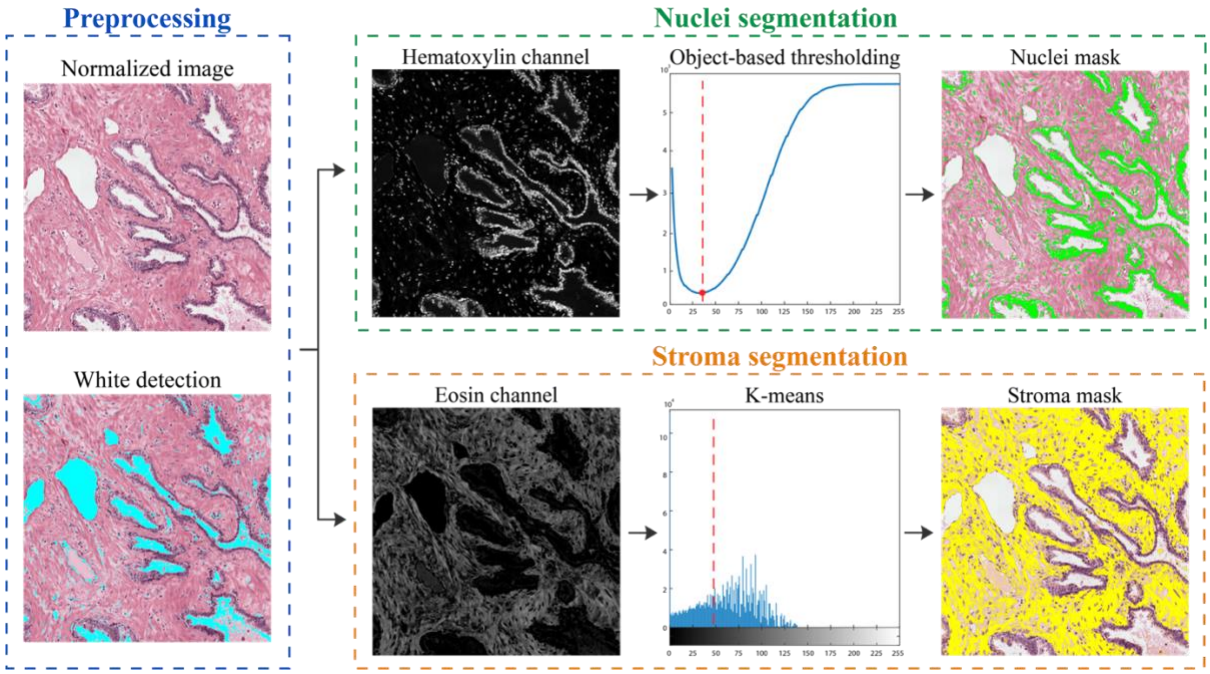

Figure 4. Object detection performed by the proposed method. White areas are first detected using a fixed threshold. Then, stain separation is performed to isolate the contribution of hematoxylin (nuclei) and eosin (stroma). Nuclei are segmented through a custom-based object thresholding, while stromal areas are found by applying a k-means clustering.

3.4 Hybrid segmentation

As can be seen from Figure S2, the semantic segmentation of CNN does not guarantee satisfactory detection of all glandular areas. The CNN output may contain false-positive shapes or incomplete glands contours. Since the direct segmentation of prostate glands is a challenging task [24], the RINGS algorithm employed a novel stroma-based approach based on identifying all the stromal areas, which in practice is finding everything that is not a gland. In this way, the glands background is found, and more accurate gland detection is achieved by complementing the stroma segmentation. Stroma detection is an easier task compared to gland detection due to the high variability of glandular patterns, especially in pathological conditions. In order to detect all the stromal regions, an RGB image combining the structure-based detection and CNN output is created. This image is called RGB_{FUSION} and contained the following elements:

1) *1st layer (red)*: CNN softmax of the "glands" class (i.e., regions inside prostate glands);
2) *2nd layer (green)*: CNN softmax of the "glands boundaries" class;
3) *3rd layer (blue)*: eosin channel obtained after contrast enhancement (saturation of the bottom 1% and the top 1% of all pixel values), where the white regions not detected by the CNN are set to 1.

In this way, the stroma/background regions have a blue tint while the regions near the edge and inside glandular areas have green and red tint, respectively. The RGB_{FUSION} is a hybrid image that contains information both from deep learning techniques (UNET) and traditional techniques (eosin channel). Compared to the original specimen, the RGB_{FUSION} image shows higher contrast between glands and stroma (Figure 5).

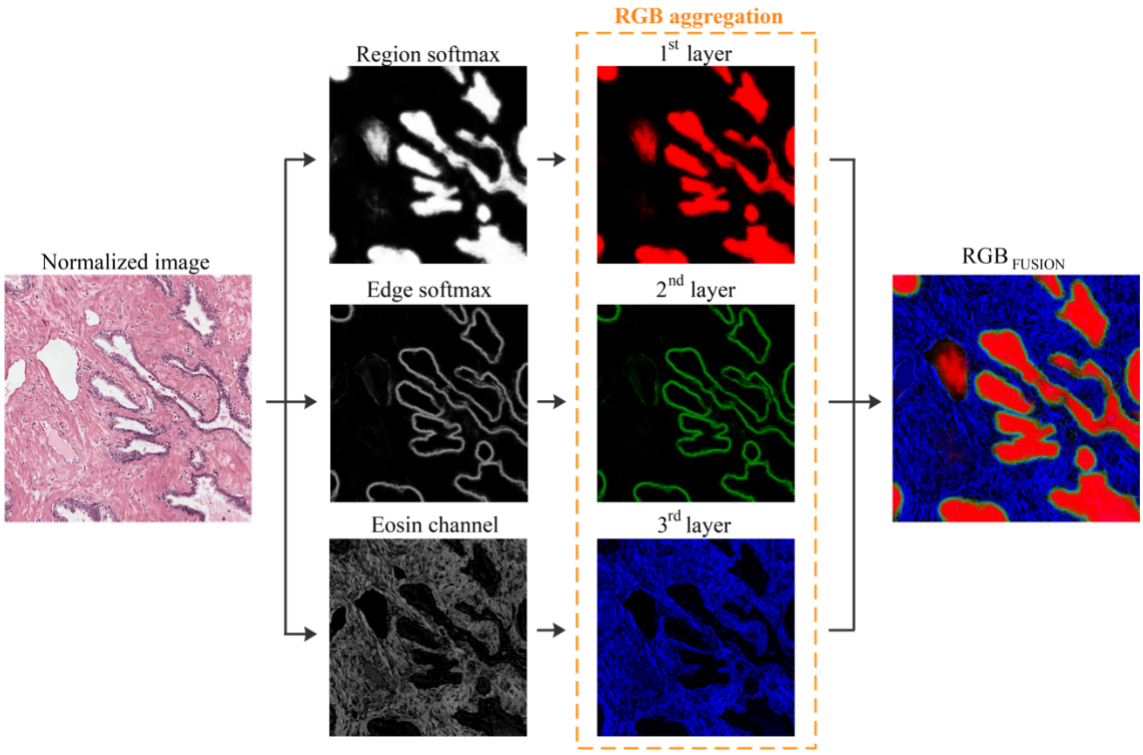

Figure 5. Procedure for obtaining the RGB_{FUSION} image. The red layer contains the softmax of the "glands" class, the green layer contains softmax of the "glands boundaries" class, while the blue layer is composed by the eosin channel after contrast enhancment.

The RINGS algorithm employs a softmax-driven active contour model on the RGB_{FUSION} image to detect all the stromal areas. Specifically, the energy model of Chan-Vese is implemented as described in Ref [39]. The Chan-Vese active contour take advantage of level sets [40], curve evolution, and energy functional to perform image segmentation. A modified version of the Mumford–Shah functional [41] is defined for the detection of all the stromal regions:

$$F = \alpha \cdot |\Gamma| + \beta \int_{\Gamma} (xdy - ydx) + \lambda_1 \cdot \int_{\Omega_{in}} |I(x,y) - \mu_{in}|^2 + \lambda_2 \cdot \int_{\Omega_{out}} |I(x,y) - \mu_{out}|^2 \qquad (4)$$

where Γ denotes the curve; Ω_{in} and Ω_{out} represent the regions inside and outside the curve; μ_{in} and μ_{out} are the mean intensity of the pixels inside and outside the curve. The parameters of the active contour model were optimized by maximizing the performance on the training set ($\alpha = 0.25, \beta = 0.05, \lambda_1 = 1.0, \lambda_2 = 1.0$). The level-set curve is initialized using the stroma mask identified in Section 3.3.2, in which all the gland pixels detected by CNN have been removed. In this way, it is possible to maintain a high sensitivity since the initial contour of the curve is always

outside the prostate glands. Before applying the active contour model, the RGB_{FUSION} image is downscaled (scale factor: 0.5) to speed up the segmentation process. The number of iterations of the Chan-Vese model is set to 40. With a low number of iterations (< 40), the model fails to adapt itself to the glands contours and, as a result, the RINGS algorithm does not perform an accurate segmentation of the glands boundaries. On the other hand, high iteration values (> 40) cause a rise in the computational time without leading to an increase in segmentation performance. The results after the level-set are illustrated in Figure 6. This hybrid segmentation approach combines the accuracy of an active contour model with the high-level features extracted by CNNs.

At the end of the level-set, the results obtained are still sub-optimal, so further steps are performed to remove all the regions that do not contain the prostate glands. Firstly, all the areas lower than 25 μm^2 composed of nuclei (isolated cells within the stroma) are removed. Then, the result of the active contour model is merged with the segmentation provided by the UNET to increase the overall performance of the proposed strategy. Finally, a structural cleaning is performed by removing all the detected shapes with a lumen percentage higher than 95% as they represent vessels or other tissue artifacts. The last step of the RINGS algorithm is the interpolation of glands boundaries through the Savitzky-Golay filter [42] with a window size of 101 pixels and polynomial order of 5. Figure 6 shows the final result provided by our segmentation method.

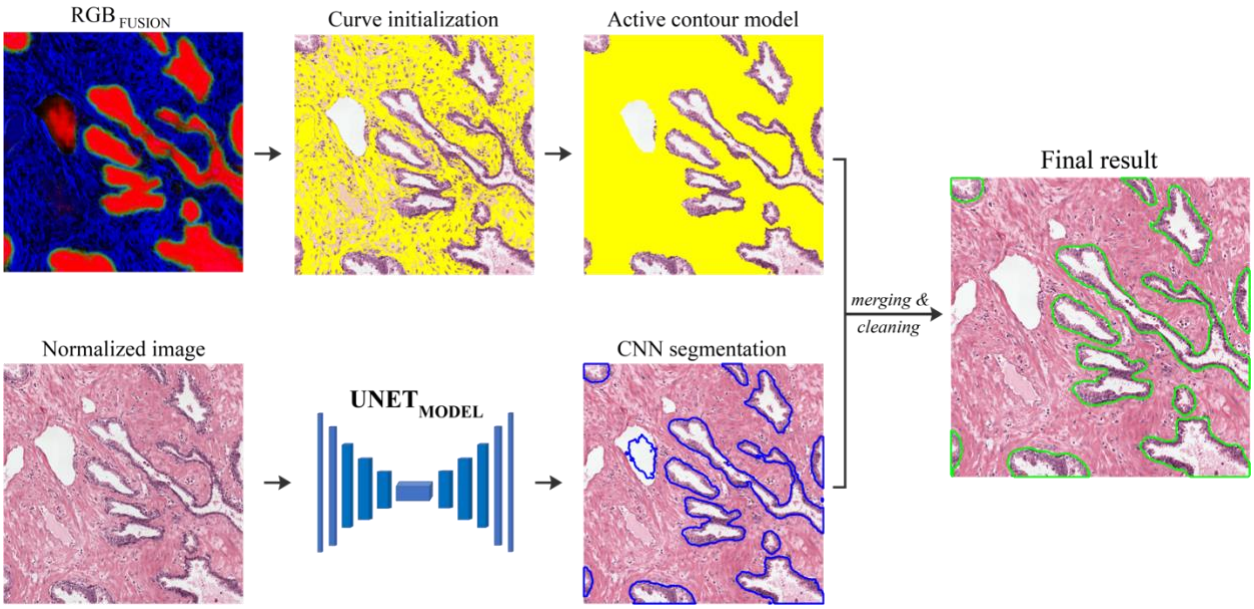

Figure 6. Hybrid segmentation approach for glands segmentation. An active contour model is applied to the RGB_{FUSION} image to accurately segment all the stromal areas. Then, the result of the active contour is merged with the

segmentation provided by the UNET. Finally, a structural cleaning is performed by removing all the regions with a high percentage of white.

3.5 Performance metrics

Automatic masks are compared with manual ones to evaluate the performance of our strategy in the segmentation of prostate glands. Several pixel-based metrics, such as balanced accuracy, precision, recall, and dice score are calculated to assess the segmentation performance. Balanced accuracy ($Bal_{ACCURACY}$) is a common metric used in segmentation problems to deal with imbalanced datasets (TP vs. TN). $Bal_{ACCURACY}$ is calculated as the average of the correct predictions of each class individually. Precision measures the false detection of ghost shapes; recall assesses the missed detection of ground truth objects; and finally, dice score measures the spatial overlap between two binary shapes [43]. For each image of the dataset, the pathologist also annotated the contour of prostate cancer. In this way, it is possible to assess the performance of the proposed method in both healthy and cancerous areas. An ideal gland detection algorithm should maintain high performance especially in tumor areas where segmentation is generally more challenging. For this reason, we evaluated the dice score for glands on healthy tissue ($dice_{HEALTHY}$) and cancer tissue ($dice_{TUMOR}$).

4. Results

4.1 Glands segmentation

The fully automated results provided by the RINGS method are compared both with manual masks drawn by an expert operator and with previously published works [18], [19], [20], [21], [22], [23], [24]. We reproduced the pipeline described in each ‘Materials and Methods' section to implement all the published algorithms. A quantitative comparison is carried out by evaluating the balanced accuracy, precision, recall, and dice score in the segmentation of prostate glands. To demonstrate the superiority of our strategy, we also evaluate the results obtained using the three-class UNET without the stain normalization (CNN no pre-processing) and the three-class UNET without the hybrid segmentation (CNN no post-processing). The entire processing is performed on a workstation with 32 GB of RAM and a 3.5 GHz octa-core CPU. Table 2 show the comparison of the proposed algorithm and current state-of-the-art methods using TRAIN and TEST datasets, respectively.

Table 2 Comparison of RINGS algorithm with current state-of-the-art methods (pixel-based metrics).

Method	Subset	Comp. Time (s)	$Bal_{ACCURACY}$	Precision	Recall	Dice
Farjam et al. [18]	TRAIN	**1.41 ± 0.07**	0.6552 ± 0.1489	0.7253 ± 0.3033	0.4566 ± 0.1795	0.5224 ± 0.2109
	TEST	**1.53 ± 0.03**	0.6378 ± 0.1586	0.7183 ± 0.3034	0.4372 ± 0.1736	0.5070 ± 0.2059
Naik et al. [19]	TRAIN	9.13 ± 1.03	0.7520 ± 0.1136	0.7253 ± 0.3033	0.4566 ± 0.1795	0.5224 ± 0.2109
	TEST	9.41 ± 1.08	0.7402 ± 0.1151	0.7958 ± 0.2021	0.5819 ± 0.2275	0.6357 ± 0.2105
Peng et al. [20]	TRAIN	2.97 ± 0.31	0.8020 ± 0.1528	0.6573 ± 0.2577	0.9420 ± 0.0935	0.7441 ± 0.2182
	TEST	2.59 ± 0.25	0.7957 ± 0.1535	0.6508 ± 0.2568	0.9305 ± 0.1124	0.7334 ± 0.2198
Nguyen et al. [21]	TRAIN	4.41 ± 0.39	0.7773 ± 0.1631	0.8416 ± 0.1360	0.7143 ± 0.2907	0.7291 ± 0.2438
	TEST	4.32 ± 0.42	0.7703 ± 0.1632	0.8260 ± 0.1588	0.7041 ± 0.2998	0.7145 ± 0.2556
Singh et al. [22]	TRAIN	8.73 ± 0.84	0.6853 ± 0.1270	0.9012 ± 0.1816	0.4115 ± 0.2483	0.5203 ± 0.2517
	TEST	8.57 ± 0.76	0.6734 ± 0.1247	0.9001 ± 0.1743	0.3869 ± 0.2493	0.4931 ± 0.2557
Ren et al. [23]	TRAIN	17.32 ± 1.98	0.8722 ± 0.1040	0.8265 ± 0.1467	0.8923 ± 0.1605	0.8394 ± 0.1382
	TEST	17.43 ± 1.91	0.8576 ± 0.1139	0.8199 ± 0.1638	0.8861 ± 0.1673	0.8308 ± 0.1495
Xu et al. [24]	TRAIN	12.45 ± 2.35	0.8379 ± 0.1052	0.7410 ± 0.1571	0.9323 ± 0.1080	0.8106 ± 0.1257
	TEST	11.84 ± 2.43	0.8250 ± 0.1106	0.7407 ± 0.1597	0.9273 ± 0.1079	0.8079 ± 0.1264
CNN no pre-processing[1]	TRAIN	9.74 ± 1.71	0.9283 ± 0.0485	0.8974 ± 0.0919	0.9148 ± 0.0797	0.8869 ± 0.0748
	TEST	9.72 ± 1.65	0.9186 ± 0.0623	0.8875 ± 0.1132	0.9157 ± 0.0952	0.8948 ± 0.0992
CNN no post-processing[2]	TRAIN	9.78 ± 1.69	0.9301 ± 0.0539	**0.9283 ± 0.0712**	0.8967 ± 0.1035	0.8924 ± 0.0795
	TEST	9.91 ± 1.56	0.9192 ± 0.0682	**0.9228 ± 0.0921**	0.8795 ± 0.1293	0.8965 ± 0.1065
RINGS algorithm	TRAIN	10.64 ± 2.11	**0.9417 ± 0.0520**	0.8860 ± 0.1379	**0.9492 ± 0.0725**	**0.9073 ± 0.0989**
	TEST	10.29 ± 2.06	**0.9325 ± 0.0684**	0.8897 ± 0.1359	**0.9356 ± 0.0964**	**0.9016 ± 0.1087**

[1] CNN with the same architecture shown in Figure 3 but trained on original images. [2] CNN trained on normalized images but without the stroma-based post-processing (section 3.4).

Our strategy exhibits excellent performances in segmenting prostate glands. The high recall (94.92% on TRAIN and 93.56% on TEST) coupled with low standard deviation values demonstrates the robustness of the proposed algorithm. A recall value close to 1 also confirms that the RINGS algorithm does not miss any prostate glands, which is extremely important in pathological conditions. Our method also obtains the best accuracy, recall, and dice for both the TRAIN and TEST sets. A large margin is achieved by RINGS compared to the state-of-the-art techniques. The suggested approach outperforms present state-of-the-art methods using the TEST set, obtaining a dice score of 90.16%. The RINGS algorithm is slightly faster than the previous deep learning methods [23], [24] (10.64 s vs. 12.75 s). More interestingly, the hybrid segmentation adopted for glands segmentation allows to further increase the performance of the single deep

network (CNN no post-processing vs. RINGS) with only 0.86 s of additional processing. To demonstrate that the joint effort between stain normalization, CNN, and active contour yields better results than the single approach, a pairwise t-test is applied between the performance of the RINGS algorithm and the "CNN no-pre-processing" and "CNN no post-processing" strategies. All statistical tests are carried out with a significance level (p) of 0.05. The paired t-test reveals a significant difference in balance accuracy and dice score for both TRAIN and TEST set (Figure 7).

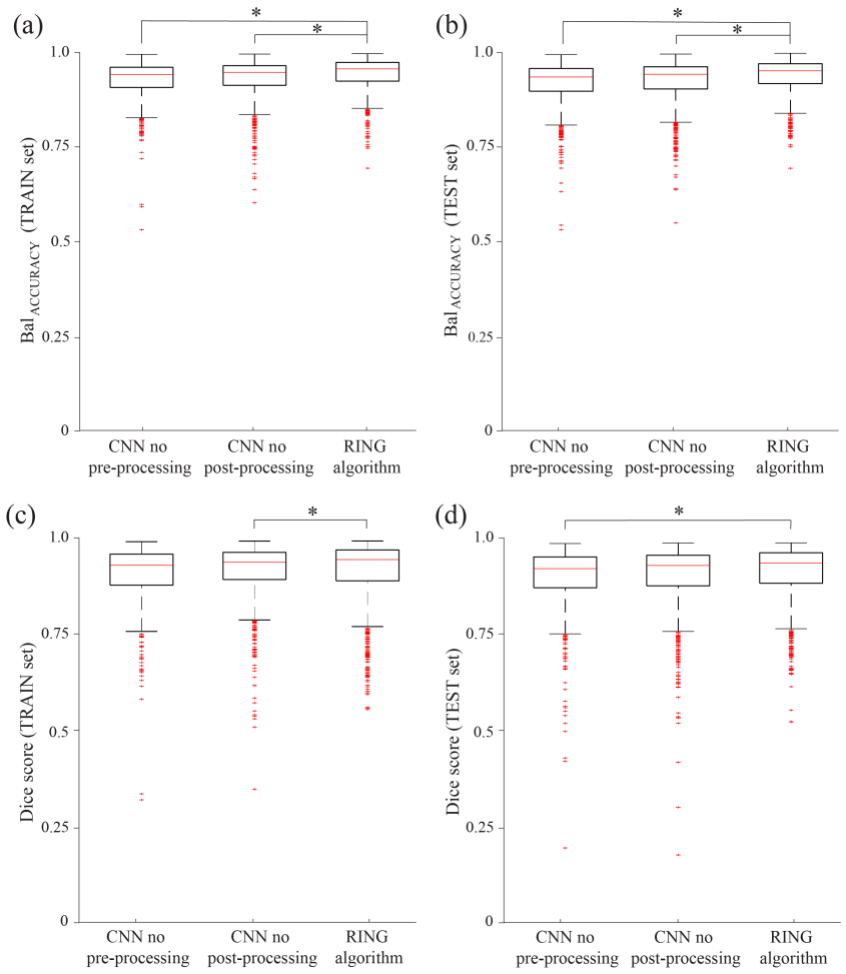

Figure 7. Comparison between RINGS performance and the three-class UNET without the stain normalization (CNN no pre-processing) and the three-class UNET without the hybrid segmentation (CNN no post-processing). (a) balanced accuracy in TRAIN set, (b) balanced accuracy in TEST set, (c) dice score in TRAIN set, (d) dice score in TEST set. Asterisk denotes statistically significant difference ($p<0.05$).

The performance of the best two published methods is shown in Figure 8 while the comparison with all other methods is reported in Figure S8. As can be seen from the Figure 8, deep learning

methods such as [23] and [24] approach the overall performance of our method but do not allow an accurate segmentation of the gland contours. By combining an active contour model with semantic segmentation, the RINGS algorithm is able to outperform all the other methods.

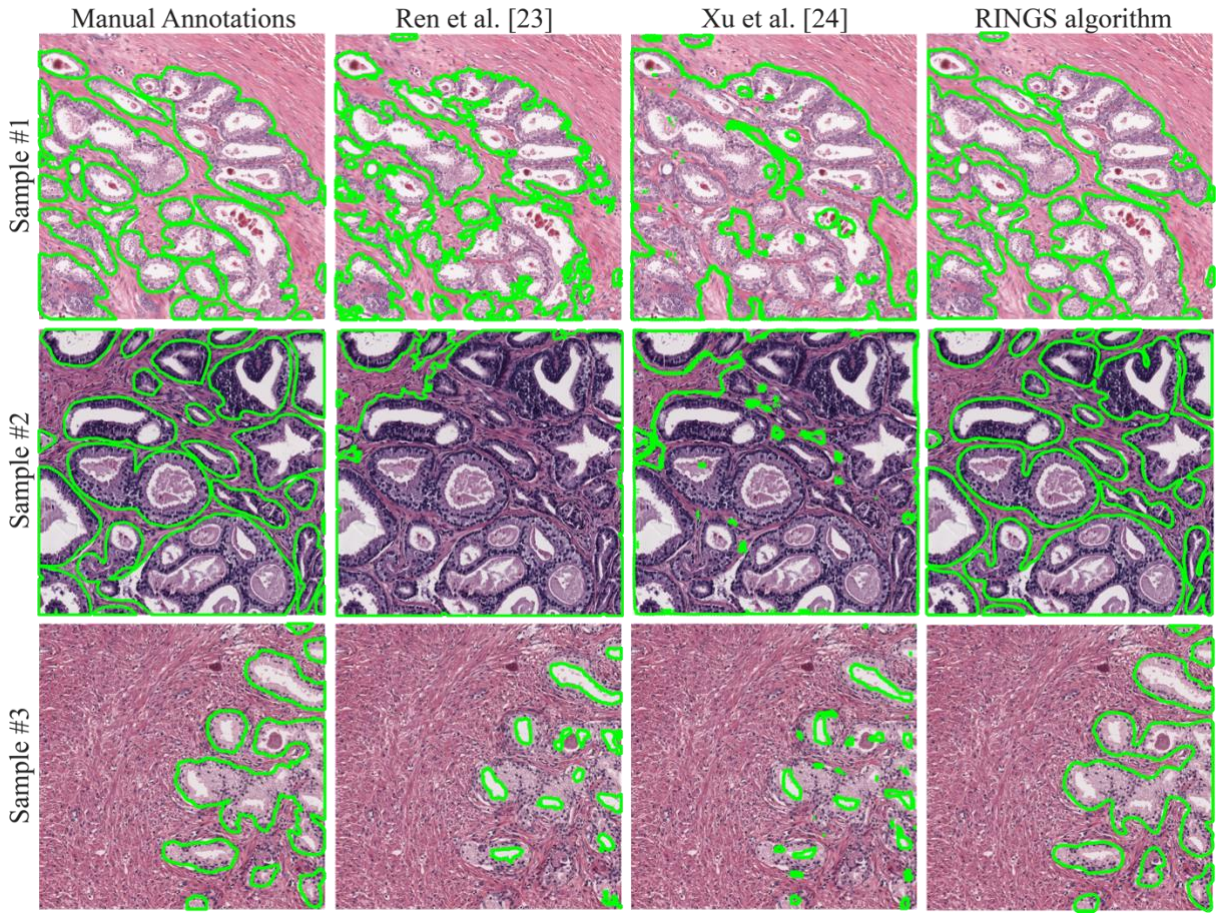

Figure 8. Performance between RINGS algorithm and the best two published deep learning methods. Each row represents sub-images taken from different samples while segmentation results are reported in columns. The original image along with manual annotations is displayed in the first column. Compared methods are shown in the second and third column, while the results of our strategy is presented in the last column.

4.2 Pathological structures

To evaluate the performance of RINGS algorithm during the segmentation of pathological structures, the dice score on healthy tissue ($Dice_{HEALTHY}$) and cancer tissues ($Dice_{TUMOR}$) are also evaluated. The RING algorithm obtains the highest dice score while segmenting tumoral glands, thus demonstrating the robustness of the proposed approach (Table 3).

Table 3 Overall performance for healthy and pathological structures using TRAIN and TEST datasets.

Method	TRAIN		TEST	
	$\mathbf{Dice_{HEALTHY}}$	$\mathbf{Dice_{TUMOR}}$	$\mathbf{Dice_{HEALTHY}}$	$\mathbf{Dice_{TUMOR}}$
Farjam et al. [18]	0.6251	0.3947	0.6128	0.4038
Naik et al. [19]	0.7549	0.5232	0.7387	0.5129
Peng et al. [20]	0.7570	0.8619	0.7402	0.8580
Nguyen et al. [21]	0.8238	0.6536	0.79001	0.6523
Singh et al. [22]	0.6725	0.2713	0.6526	0.2525
Ren et al. [23]	0.8730	0.8666	0.8699	0.8485
Xu et al. [24]	0.8674	0.8540	0.8632	0.8402
CNN no pre-processing[1]	0.9034	0.8836	0.9104	0.8934
CNN no post-processing[2]	**0.9204**	0.8911	0.9058	0.8751
RINGS algorithm	0.9113	**0.9088**	**0.9103**	**0.8987**

[1] CNN with the same architecture shown in Figure 3 but trained on original images. [2] CNN trained on normalized images but without the stroma-based post-processing (section 3.4).

A visual comparison between state-of-the-art methods and the proposed one for different pathological structures is shown in Figure 9. Being based on stroma segmentation, no performance degradation is observed when segmenting healthy or pathological structures. The RINGS algorithm is able to correctly detect the glands contours even in the presence of severe glandular degeneration (Figure 9 – Sample #1). The combination of semantic segmentation and level-set is able to detect prostate glands with discontinuous and absence of lumina accurately (Figure 9 – Sample #2).

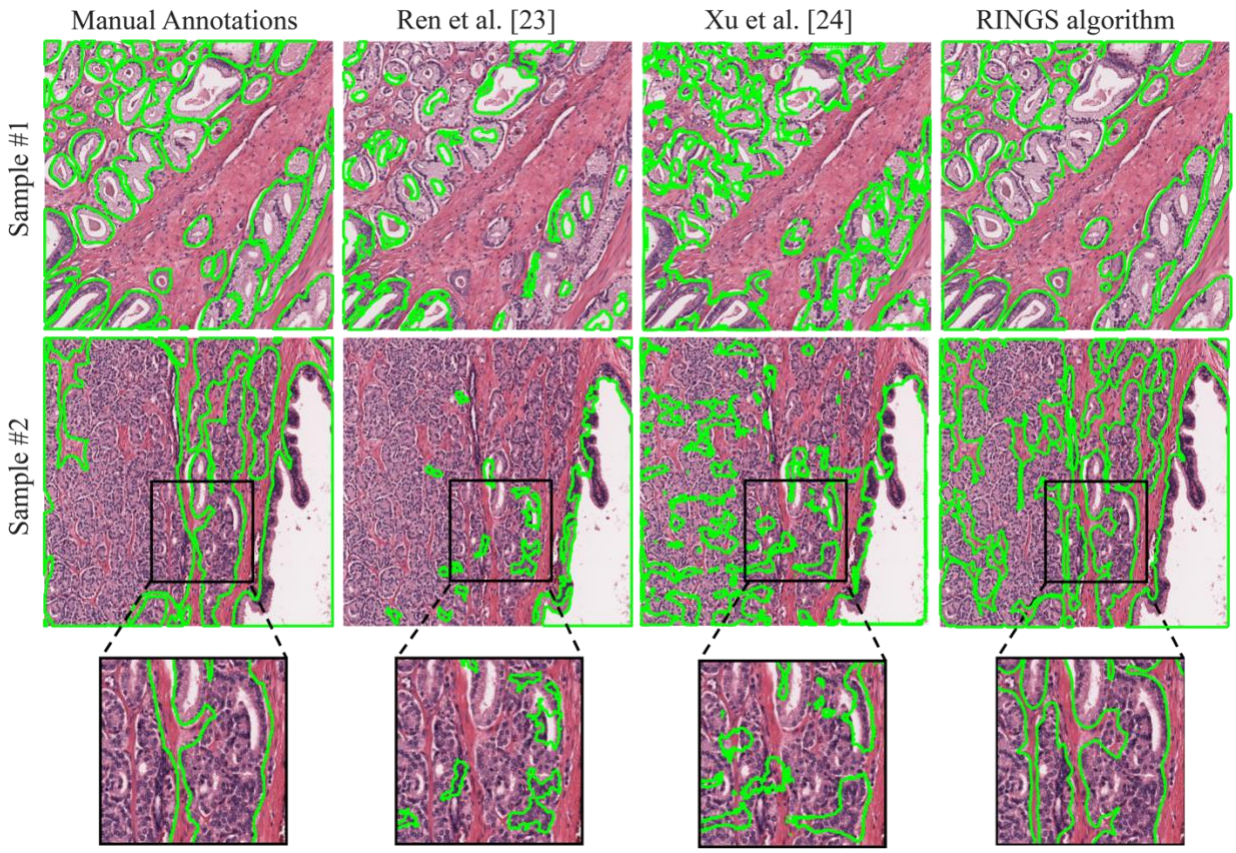

Figure 9. Performance between the best two published deep learning algorithm and our strategy for different pathological structures. First column illustrates the manual segmentation, while the second and third columns show the comparison with other best methods. Last column shows the results of the proposed algorithm.

4.3 Extension to other datasets

Since prostate glands are generally assessed on tissue microarrays (TMAs) and whole slide images (WSIs), we have extended our strategy to entire biopsies using a sliding window approach. In particular, we used a public database of prostatic TMAs [44] and a set of proprietary histological slides to test our strategy on two different external datasets. Before testing the RINGS algorithm, we normalized each image of these two datasets according to our chosen reference H&E-stained image (Figure 2b). Then, we applied our algorithm as is, without applying any changes to its parameters. Figure 10a and 10b illustrate the results obtained on three TMAs and a biopsy, respectively. To evaluate the architecture of prostate glands, an expert pathologist takes at least 10 min per slide, while the RINGS algorithm is able to process the entire WSI in about 3 min. The introduction of an automatic algorithm within the clinical workflow can speed up the diagnostic process and provide more accurate data to assess prostate cancer.

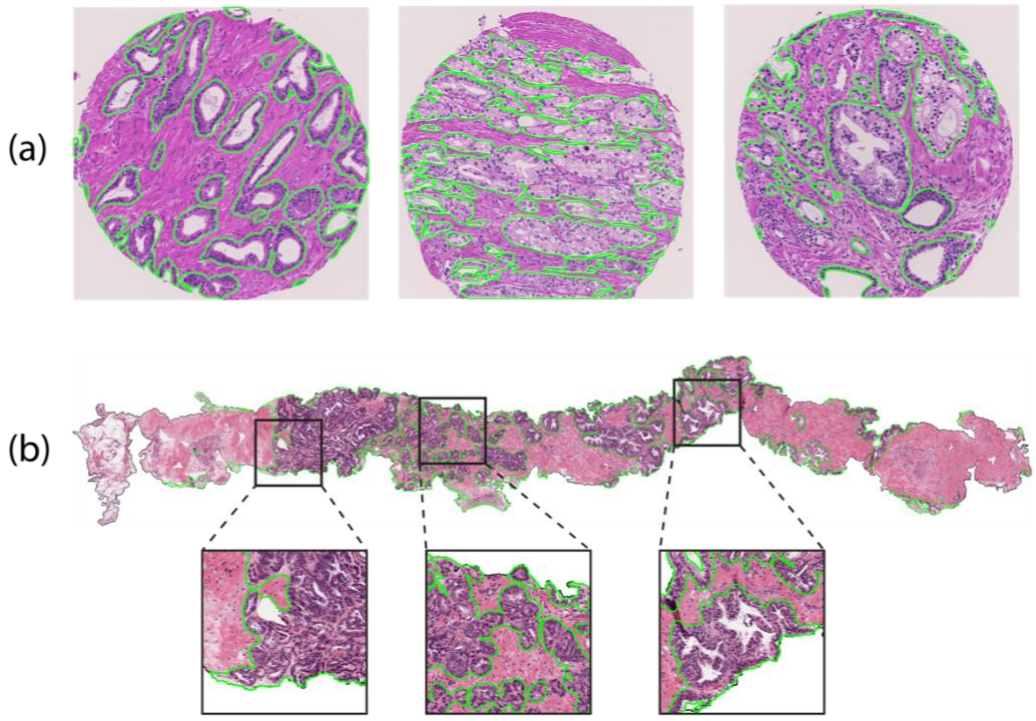

Figure 10. Result of RINGS processing on (a) three public TMAs [44] and on (b) a biopsy acquired at Città della Salute e della Scienza Hospital (Turin, Italy). The detected prostate glands are shown in green.

4.4 CAD for cancer detection

Recent studies demonstrated that an accurate glands segmentation is a useful preprocessing step to improve the performance of computer-aided diagnosis (CAD) system for cancer detection [14], [45]. If the automated algorithm has high recall rate, the CNN can be applied only on the detected glandular regions. In this way, all structures of not interest (e.g., stroma, vessels, etc.) are excluded from the classification, thus reducing both the computational time and false-positive results. Chen et al. [14] have demonstrates that training a CNN only on glandular regions (i.e., where prostate cancer occurs) leads to a 26.9% improvement in cancer detection accuracy. For this reason, we have conducted experiments to evaluate the improvement of CNN model using different methods of gland segmentation (Figure S9). In particular, a GoogleNet architecture [46] is trained using our TRAIN dataset (1000 images) and validated using the TEST set (500 images). For each image of our dataset, an expert pathologist (M.B.) also annotated the contour of prostate cancer. These contours were used to train and test the CNN. The encoding network was pre-trained

on ILSVRC 2012 ImageNet [35] and the Adam optimizer was employed with an initial learning rate of 0.001. The training was performed on a dedicated workstation with 128 GB of RAM and a 4.1 GHz ten-core CPU using Keras framework and TensorFlow as backend. Table 4 summarizes all the results obtained. The RINGS algorithm is able to increase the quality of a CAD system designed for cancer detection, obtaining the best precision rate of 91.24% and recall rate of 97.23% in cancer detection. At the same time, the computational time is reduced by more than 25% compared to other methods.

Table 4 Performance of CAD for cancer detection using different glands segmentation method as preprocessing steps.

Method	Comp. Time (s)	Precision	Recall
No preprocessing	1.74 ± 0.06	0.6862	0.5825
Farjam et al. [18]	1.02 ± 0.27	0.7841	0.6207
Naik et al. [19]	0.87 ± 0.23	0.8235	0.6934
Peng et al. [20]	0.79 ± 0.21	0.6927	0.9568
Nguyen et al. [21]	0.74 ± 0.29	0.8441	0.7471
Singh et al. [22]	0.95 ± 0.31	0.9087	0.6519
Ren et al. [23]	0.58 ± 0.18	0.8873	0.8921
Xu et al. [24]	0.64 ± 0.20	0.7927	0.9247
CNN no pre-processing[1]	0.55 ± 0.17	0.8958	0.9624
CNN no post-processing[2]	0.56 ± 0.09	0.9105	0.9371
RINGS algorithm	**0.53 ± 0.11**	**0.9124**	**0.9723**

[1] CNN with the same architecture shown in Figure 3 but trained on original images. [2] CNN trained on normalized images but without the stroma-based post-processing (section 3.4).

5. Discussion and Conclusions

Study of prostatic cancer has been a challenging task in the field of pathology due to its complex glandular structure. The main challenge is the accurate classification of heterogeneous tumors which presents several architectural patterns correlated with tumor aggressiveness and prognostic outcomes [47], [48]. Finally, Gleason score system is proposed after many years of hard work by researchers in this area. The International Society of Urologist and Pathologist (ISUP) has made *two* radical updates to the Gleason score. They introduced Gleason grading - a clarifying and simplified grouping system to the Gleason score with enriched prognostic correlation. But the inter- and intra-subjectivity and grading variability are still far from their best.

In this puzzling scenario, every improvement in recognizing gland architecture and correctly classified it is of mandatory importance.

In this study, we present a novel strategy for automated prostate glands segmentation in histopathological images. Detection of glands is a real challenge due to the variability of the size, shape and internal architecture of the glands. Thanks to the stain normalization step, our algorithm is capable of automatically detecting prostate glands in images with different staining intensity. The proposed approach is tested on 500 H&E stained images of prostate tissue and results are compared with manual annotations by an expert pathologist. Our method shows the highest accuracy, recall and dice compared to state-of-the-art techniques in both TRAIN and TEST dataset. More importantly, our method obtains the highest recall rate (TRAIN: 94.92%, TEST: 93.56%) as compared to the current published methods. This means that the proposed algorithm generated the lowest false negative rate compared to the other techniques. As can be seen from Figure 9, the algorithm maintained high performance even in the presence of severe glandular degeneration, thus demonstrating the robustness of the proposed approach.

These high performances are mainly due to the combination of an accurate object detection (lumen, nuclei and stroma detection) coupled with high-level features extraction using deep learning techniques (UNET). Starting from stroma segmentation, our method is able to identify the gland boundaries by complementing the detected stromal regions. Using this indirect strategy, RINGS algorithm is able to bypass all the issues of the current state-of-the-art methods (see Section 2). The stain normalization step is fundamental to standardize the intensity of the stromal regions and make the softmax-driven active contour model more stable and performing. The proposed pipeline also integrated a post-processing refining to remove the detected false-positive shapes (e.g., broken tissue areas, isolated cell nuclei, vessels, etc.). The limitation of RINGS algorithm is related to the stain content: if the eosin is not present in the image, stroma segmentation may fail, and the entire pipeline can yield suboptimal results. On the other hand, prostate cancer is generally assessed on biopsies (Figure 10b), so there is always a small amount of stroma to initialize the active contour model. In addition, histological images should be acquired at 5x or greater magnification: using a lower resolution, the cellular structures segmentation may fail due to poor quality images.

Being based on stroma segmentation, the proposed methodology can be easily extended in the future to other histological structures (e.g., tubule, epithelium) or tissues (e.g., colon, breast). In

addition, we are planning to extend our dataset with images acquired from multiple centers and different types of scanners to further increase the robustness of the RINGS algorithm. Our research group is currently working on the extension of RINGS algorithm for entire prostate biopsy with an aim to develop a faster and accurate automated Gleason grading system.

Acknowledgments

The authors would like to acknowledge all the laboratory technicians of the Division of Pathology (Department of Oncology, Turin, Italy) for their help in digitizing histological.

CRediT authorship contribution statement

Massimo Salvi: Methodology, Software, Writing – Original Draft. **Martino Bosco**: Data Curation, Resources. **Luca Molinaro**: Investigation, Resources. **Alessandro Gambella**: Writing - Review & Editing. **Mauro Papotti**: Supervsion. **U Rajendra Acharya**: Validation, Writing - Review & Editing. **Filippo Molinari**: Conceptualization, Supervision.

References

[1] Pernar CH, Ebot EM, Wilson KM, Mucci LA. The epidemiology of prostate cancer. Cold Spring Harb Perspect Med 2018;8:a030361.

[2] Rawla P. Epidemiology of prostate cancer. World J Oncol 2019;10:63.

[3] Narayan V, Jiang S, Warlick CA. Early Stage Cancer in Older Adults: Prostate—Avoiding Overtreatment and Undertreatment. Cancer J 2017;23:238–41.

[4] Gnanapragasam VJ, Bratt O, Muir K, Lee LS, Huang HH, Stattin P, et al. The Cambridge Prognostic Groups for improved prediction of disease mortality at diagnosis in primary non-metastatic prostate cancer: a validation study. BMC Med 2018;16:31.

[5] Daskivich TJ, Fan K-H, Koyama T, Albertsen PC, Goodman M, Hamilton AS, et al. Prediction of long-term other-cause mortality in men with early-stage prostate cancer: results from the Prostate Cancer Outcomes Study. Urology 2015;85:92–100.

[6] Ozkan TA, Eruyar AT, Cebeci OO, Memik O, Ozcan L, Kuskonmaz I. Interobserver variability in Gleason histological grading of prostate cancer. Scand J Urol 2016;50:420–4.

[7] Rodriguez-Urrego PA, Cronin AM, Al-Ahmadie HA, Gopalan A, Tickoo SK, Reuter VE, et al. Interobserver and intraobserver reproducibility in digital and routine microscopic assessment of prostate needle biopsies. Hum Pathol 2011;42:68–74.

[8] Allsbrook Jr WC, Mangold KA, Johnson MH, Lane RB, Lane CG, Epstein JI. Interobserver

reproducibility of Gleason grading of prostatic carcinoma: general pathologist. Hum Pathol 2001;32:81–8.

[9] Sadimin ET, Khani F, Diolombi M, Meliti A, Epstein JI. Interobserver reproducibility of percent Gleason pattern 4 in prostatic adenocarcinoma on prostate biopsies. Am J Surg Pathol 2016;40:1686–92.

[10] Zhou M, Li J, Cheng L, Egevad L, Deng F-M, Kunju LP, et al. Diagnosis of "Poorly Formed Glands" Gleason Pattern 4 Prostatic Adenocarcinoma on Needle Biopsy. Am J Surg Pathol 2015;39:1331–9.

[11] Meliti A, Sadimin E, Diolombi M, Khani F, Epstein JI. Accuracy of grading Gleason score 7 prostatic adenocarcinoma on needle biopsy: influence of percent pattern 4 and other histological factors. Prostate 2017;77:681–5.

[12] Zietman A, Smith J, Klein E, Droller M, Dasgupta P, Catto J. Consensus guidelines for reporting prostate cancer Gleason grade. Urology 2016;93:1.

[13] Zietman A, Smith J, Klein E, Droller M, Dasgupta P, Catto J. Describing the Grade of Prostate Cancer: Consistent Use of Contemporary Terminology Is Now Required. Eur Urol 2016;70:1.

[14] Chen C, Huang Y, Fang P, Liang C, Chang R. A computer-aided diagnosis system for differentiation and delineation of malignant regions on whole-slide prostate histopathology image using spatial statistics and multidimensional DenseNet. Med Phys 2020;47:1021–33.

[15] Rezaei S, Emami A, Zarrabi H, Rafiei S, Najarian K, Karimi N, et al. Gland segmentation in histopathology images using deep networks and handcrafted features. 2019 41st Annu. Int. Conf. IEEE Eng. Med. Biol. Soc., IEEE; 2019, p. 1031–4.

[16] Sirinukunwattana K, Pluim JPW, Chen H, Qi X, Heng P-A, Guo YB, et al. Gland segmentation in colon histology images: The glas challenge contest. Med Image Anal 2017;35:489–502.

[17] Qu H, Yan Z, Riedlinger GM, De S, Metaxas DN. Improving nuclei/gland instance segmentation in histopathology images by full resolution neural network and spatial constrained loss. Int. Conf. Med. Image Comput. Comput. Interv., Springer; 2019, p. 378–86.

[18] Farjam R, Soltanian-Zadeh H, Jafari-Khouzani K, Zoroofi RA. An image analysis approach for automatic malignancy determination of prostate pathological images. Cytom Part B Clin Cytom J Int Soc Anal Cytol 2007;72:227–40.

[19] Naik S, Doyle S, Agner S, Madabhushi A, Feldman M, Tomaszewski J. Automated gland and nuclei segmentation for grading of prostate and breast cancer histopathology. 2008 5th IEEE Int. Symp. Biomed. Imaging From Nano to Macro, IEEE; 2008, p. 284–7.

[20] Peng Y, Jiang Y, Eisengart L, Healy MA, Straus FH, Yang XJ. Computer-aided identification of prostatic adenocarcinoma: Segmentation of glandular structures. J Pathol Inform 2011;2.

[21] Nguyen K, Sabata B, Jain AK. Prostate cancer grading: Gland segmentation and structural features. Pattern Recognit Lett 2012;33:951–61.

[22] Singh M, Kalaw EM, Giron DM, Chong K-T, Tan CL, Lee HK. Gland segmentation in prostate histopathological images. J Med Imaging 2017;4:027501.

[23] Ren J, Sadimin E, Foran DJ, Qi X. Computer aided analysis of prostate histopathology images to support a refined Gleason grading system. Med. Imaging 2017 Image Process., vol. 10133, International Society for Optics and Photonics; 2017, p. 101331V.

[24] Xu Y, Li Y, Wang Y, Liu M, Fan Y, Lai M, et al. Gland instance segmentation using deep multichannel neural networks. IEEE Trans Biomed Eng 2017;64:2901–12.

[25] Zeng N, Zhang H, Song B, Liu W, Li Y, Dobaie AM. Facial expression recognition via learning deep sparse autoencoders. Neurocomputing 2018;273:643–9.

[26] Zeng N, Wang Z, Zhang H, Kim K-E, Li Y, Liu X. An improved particle filter with a novel hybrid proposal distribution for quantitative analysis of gold immunochromatographic strips. IEEE Trans Nanotechnol 2019;18:819–29.

[27] Zeng N, Li H, Wang Z, Liu W, Liu S, Alsaadi FE, et al. Deep-Reinforcement-Learning-Based Images Segmentation for Quantitative Analysis of Gold Immunochromatographic Strip. Neurocomputing 2020.

[28] Madabhushi A, Lee G. Image analysis and machine learning in digital pathology: Challenges and opportunities 2016.

[29] Janowczyk A, Madabhushi A. Deep learning for digital pathology image analysis: A comprehensive tutorial with selected use cases. J Pathol Inform 2016;7.

[30] Song J, Xiao L, Molaei M, Lian Z. Multi-layer boosting sparse convolutional model for generalized nuclear segmentation from histopathology images. Knowledge-Based Syst 2019;176:40–53.

[31] Salvi M, Michielli N, Molinari F. Stain Color Adaptive Normalization (SCAN) algorithm: separation and standardization of histological stains in digital pathology. Comput Methods Programs Biomed 2020:105506.

[32] Tosta TAA, de Faria PR, Neves LA, do Nascimento MZ. Computational normalization of H&E-stained histological images: Progress, challenges and future potential. Artif Intell Med 2019;95:118–32.

[33] Niethammer M, Borland D, Marron JS, Woosley J, Thomas NE. Appearance normalization of histology slides. Int. Work. Mach. Learn. Med. Imaging, Springer; 2010, p. 58–66.

[34] Ronneberger O, Fischer P, Brox T. U-Net: Convolutional Networks for Biomedical Image Segmentation, Springer, Cham; 2015, p. 234–41. https://doi.org/10.1007/978-3-319-24574-4_28.

[35] Krizhevsky A, Sutskever I, Hinton GE. Imagenet classification with deep convolutional neural

networks. Adv. Neural Inf. Process. Syst., 2012, p. 1097–105.

[36] Sarkar D, Bali R, Ghosh T. Hands-On Transfer Learning with Python: Implement advanced deep learning and neural network models using TensorFlow and Keras. Packt Publishing Ltd; 2018.

[37] Salvi M, Molinari F. Multi-tissue and multi-scale approach for nuclei segmentation in H&E stained images. Biomed Eng Online 2018;17. https://doi.org/10.1186/s12938-018-0518-0.

[38] Arthur D, Vassilvitskii S. k-means++: The advantages of careful seeding. Proc. eighteenth Annu. ACM-SIAM Symp. Discret. algorithms, Society for Industrial and Applied Mathematics; 2007, p. 1027–35.

[39] Chan TF, Vese LA. Active contours without edges. IEEE Trans Image Process 2001;10:266–77.

[40] Sethian JA, Sethian JA. Level set methods: Evolving interfaces in geometry, fluid mechanics, computer vision, and materials science. vol. 74. Cambridge university press Cambridge; 1996.

[41] Mumford D, Shah J. Optimal approximations by piecewise smooth functions and associated variational problems. Commun Pure Appl Math 1989;42:577–685.

[42] Orfanidis SJ. Introduction to Signal Processing, Prentice Hall. Englewood Cliffs, NJ 1996.

[43] Real R, Vargas JM. The probabilistic basis of Jaccard's index of similarity. Syst Biol 1996;45:380–5.

[44] Arvaniti E, Fricker KS, Moret M, Rupp N, Hermanns T, Fankhauser C, et al. Automated Gleason grading of prostate cancer tissue microarrays via deep learning. Sci Rep 2018;8:1–11.

[45] Salvi M, Acharya UR, Molinari F, Meiburger KM. The impact of pre-and post-image processing techniques on deep learning frameworks: a comprehensive review for digital pathology image analysis. Comput Biol Med 2020:104129.

[46] Shin H-C, Roth HR, Gao M, Lu L, Xu Z, Nogues I, et al. Deep convolutional neural networks for computer-aided detection: CNN architectures, dataset characteristics and transfer learning. IEEE Trans Med Imaging 2016;35:1285–98.

[47] Sahran S, Albashish D, Abdullah A, Abd Shukor N, Pauzi SHM. Absolute cosine-based SVM-RFE feature selection method for prostate histopathological grading. Artif Intell Med 2018;87:78–90.

[48] Talo M. Automated classification of histopathology images using transfer learning. Artif Intell Med 2019;101:101743.